CHARGE GENERATION BY SECONDARY PARTICLES FROM NUCLEAR REACTIONS IN BACK END OF LINE MATERIALS

By

Nathaniel Anson Dodds

Thesis

Submitted to the Faculty of the

Graduate School of Vanderbilt University

in partial fulfillment of the requirements

for the degree of

MASTER OF SCIENCE

in

Electrical Engineering

December, 2009

Nashville, Tennessee

Approved:

Professor Robert A. Reed

Professor Marcus H. Mendenhall

ACKNOWLEDGEMENTS

More than anyone else, I am indebted to my wife Stacey for her support through these years of research. From agreeing to move far from home (how far is Nashville from Phoenix?) to encouraging me to finally write this thesis, she has been my sweet companion. I owe my parents for teaching me to love learning, and for working so I could have more opportunities than they ever had.

I'm grateful to my advisor Robert Reed, for showing me how to enjoy the windy road of research. This work wouldn't have been possible without his friendship and guidance, as well as that of Marcus Mendenhall, Michael Clemens, and Robert Weller. I owe special thanks to Paul Dodd and Marty Shaneyfelt of Sandia National Laboratories for giving me the test structures used in this study.

This work was supported by the Defense Threat Reduction Agency under contracts HDTRA1-08-1-0033 and HDTRA1-08-1-0034, the NASA Electronics Parts and Packaging Program, and the NASA Graduate Student Researchers Program.

TABLE OF CONTENTS

Page

ACKNOWLEDGEMENTS ii

LIST OF TABLES iv

LIST OF FIGURES v

Chapter

I. INTRODUCTION 1

II. BACKGROUND 3

- Ionization Mechanisms 3
- Nuclear Reaction-Induced Single Event Effects 5
- Pulse Height Analysis 10

III. EXPERIMENTAL DESIGN 13

- Observability of Nuclear Events 13
- Test Structures 15
- Test Setup 17
- Heavy Ion Irradiation 21

IV. IMPACT OF THE PRESENCE AND PLACEMENT OF TUNGSTEN 23

V. IMPACT OF ION ENERGY ON CHARGE COLLECTION 26

- Data on Ion Energy Dependence 26
- Simulations Identifying Worst-Case Energy 29
- Physical Mechanism 33
- Hardness Assurance Implications 36

VI. CONCLUSIONS 38

Appendix 39

- DISCRIMINATOR BOARD DESIGN 39

REFERENCES 42

LIST OF TABLES

1. Heavy Ion Beams Used in This Work……………………………...…………………….21

LIST OF FIGURES

Figure 1: Representation of an inelastic nuclear reaction. 4

Figure 2: Representation of either a coulomb scattering event, or of an elastic nuclear reaction... 4

Figure 3: Simulated spectrum of charge deposition from 523 MeV ^{20}Ne in the sensitive volume of a certain silicon structure. Rare nuclear events are capable of depositing large amounts of charge. Taken from [3]. 6

Figure 4: Simulated integral cross section of charge deposition from 523 MeV ^{20}Ne in the sensitive volume of a certain silicon structure. If the critical charge is known then the SEE cross section can be read directly from the curve. Taken from [3]. 6

Figure 5: Measured SEU cross section for a radiation-hardened SRAM. Nuclear reactions caused upsets at LET values well below the 40 MeV·cm^2/mg SEU LET threshold of the device. Taken from [3]. 7

Figure 6: Measured SEU cross section for an SRAM. Even when testing at the same LET value, higher energy ions produce higher SEU cross sections than low energy ions. Taken from [6]...... 9

Figure 7: Block diagram of a generic pulse height analysis system. This system can be used to produce a spectrum that characterizes charge generation events in the detector. 10

Figure 8: Measured pulse height spectrum from 5.4 MeV alpha particles incident on a silicon surface barrier detector. This spectrum is used to perform an energy calibration by defining the centroid of the distribution, bin number 495, to occur at 5.4 MeV 11

Figure 9: SOI test structures containing metallization at the (a) W1 and M1 layers, (b) W2 and M2 layers, and (c) W3 and M3 layers. These and other test structures allow identification of the role of overlayer materials on charge generation in the active silicon. Not drawn to scale.......... 15

Figure 10: Block diagram of the 16-channel PHA system and auxiliary equipment. 18

Figure 11: A noise spike on the detector bias supply line caused the anomalous large-amplitude events shown in (a). These events affect multiple channels in the same digitization cycle, and were filtered from the data via post-processing, as shown in (b) 19

Figure 12: Measurement of the total number of counts during a high fluence heavy ion exposure. This non-linear curve shows that the count rate was decreasing over time, because of displacement damage in the diodes 20

Figure 13: LET can be held constant while increasing particle energy by increasing the atomic number of the ions in the beam. Circles represent the heavy ion beams used in this work. Generated using SRIM-2008 [15]. 22

Figure 14: Measured integral cross section of 40 MeV/u ^{20}Ne ions on the test structures. The presence of tungsten near the active silicon led to extreme charge collection events. 23

Figure 15: Measured SEU cross section as a function of energy at an incident effective LET of ~5 MeV·cm^2/mg. These data raise the question of whether SEU cross sections increase without bound as particle energy increases and LET is held constant. Taken from [6]............................ 27

Figure 16: The galactic cosmic ray differential energy spectra for hydrogen, helium, and iron. Taken from [16]. 27

Figure 17: Measured integral cross section from the test structures for two heavy ion beams with the same LET. The higher energy test produced smaller-amplitude charge collection events. 28

Figure 18: Measured integral cross section from the test structures for three heavy ion beams with the same LET. The higher energy test produced smaller-amplitude charge collection events. 28

Figure 19: Simulated integral cross section of various fixed-LET heavy ions on a bulk-Si device. 30

Figure 20: Simulated SEU cross section as a function of energy for a bulk-Si device. The worst-case energy, or the energy resulting in the highest SEU cross section, depends on Q_{crit}. 31

Figure 21: Simulated SEU cross section as a function of energy for an SOI device. The worst-case energy, or the energy resulting in the highest SEU cross section, depends on Q_{crit}. 32

Figure 22: Simulated nuclear spallation reactions caused by a) 40 MeV/u neon and by b) 10000 MeV/u iron. These representative events suggest that very high energy nuclear reactions produce lower-mass and higher-energy secondary particles, which therefore have lower LET. 33

Figure 23: Simulated isobaric cross section for secondary particles resulting from irradiating ^{184}W with various 1.2 MeV·cm^2/mg ions. Results suggest that higher energy incident particles cause greater decomposition of the target nucleus, producing more intermediate and low mass secondary particles. 35

Figure 24: Simulated cross section for the secondary particles produced from various 1.2 MeV·cm2/mg ions incident on ^{184}W as a function of secondary particle initial LET. Results suggest that fewer high LET secondary particles are produced when incident particle energy is increased beyond a certain point. 35

Figure 25: Block diagram of the Mesytec MPRS-16 preamplifier/shaping amplifier. The TRIGGER output (labeled NIM out) cannot be used for this application, because it is produced by summing the signals from the various channels. 40

Figure 26: Simplified diagram of the discriminator board with embedded explanations. This circuit produces a trigger signal that tells the ADC to digitize when the magnitude of a pulse on any of the 16 channels exceeds $V_{threshold}$. 41

CHAPTER I

INTRODUCTION

The focus of this thesis is to deepen our understanding of the factors affecting how nuclear reactions contribute to single event effects (SEEs) in modern integrated circuits (ICs). Factors studied include overlayer material, overlayer position, and incident particle energy.

Several papers have suggested that the presence of high atomic number (high-Z) materials, like tungsten, within the IC back end of line (BEOL), leads to extreme charge generation events through nuclear reactions. These papers rely on nuclear physics simulations [1-5] and on the analysis of anomalous circuit-level errors [1,3,4,6] to support this claim. In this work, charge collection measurements [7] were used to directly determine the role of tungsten overlayers on radiation-induced charge collection. These measurements prove that the presence of high-Z materials can lead to extreme charge collection events. Furthermore, the data show that, for the technology studied, the closer tungsten is to the sensitive volume the more efficiently nuclear reaction-induced charge is collected.

When nuclear reactions dominate the error rate, SEE cross sections have been shown to increase as particle energy is increased and linear energy transfer (LET) is held constant [1,6]. In [6], Dodd questioned whether these SEE cross sections would continue to increase as particle energy is increased to those high energies found in the galactic cosmic ray (GCR) spectrum. Thus, the ion energy dependence of nuclear reaction-induced SEEs is not well understood. In this work, heavy ion (atomic mass > 1) tests were performed over the range of 16 MeV/u to 1000 MeV/u at constant LET. The LET was held constant by using heavier ions for the higher energies. The highest energy data suggest that nuclear reaction-induced charge collection does not grow without bound as fixed-LET incident particle energy is increased, but rather reaches a

maximum at some energy and then decreases. This maximum is the worst-case energy for SEE susceptibility at that LET, and varies with device layout and technology. A simulation approach for identifying this worst-case energy is applied to certain bulk-Si and silicon-on-insulator (SOI) technologies. Nuclear physics simulations are presented, suggesting that the decrease in charge collection beyond the worst-case energy occurs because the secondary particles produced from such high-energy nuclear reactions have less mass and higher energy and are therefore less ionizing than those produced by lower-energy reactions.

CHAPTER II

BACKGROUND

Ionization Mechanisms

This section identifies the various mechanisms by which particles having at least one atomic mass unit can generate electron-hole pairs in a target material. *Direct ionization* is the classification for events in which the incident particles themselves generate charge in the target medium. *Indirect ionization* occurs when the incident particle produces secondary particles, which go on to generate charge. There are three types of indirect ionization: inelastic nuclear reactions, coulomb scattering, and elastic nuclear reactions.

Direct ionization generates electron-hole pairs through the interaction of the positively charged incident nucleus with the negatively charged electrons in the target material. The metric used to quantify direct ionization is linear energy transfer (LET). LET is traditionally measured in units of MeV·cm^2/mg. These units arise because the energy transfer per unit path length (MeV/cm) is normalized by the density of the target material (mg/cm^3).

Inelastic nuclear reactions occur when the incident particle strikes a target nucleus, causing fragmentation and the ejection of secondary particles. A cartoon of such a reaction is shown in Figure 1. *Coulomb scattering*—or Rutherford scattering—occurs when the incident particle gets close enough to the target nucleus that their positive charges cause them to repel each other through the Coulomb force. If the incident particle gets even closer to the target nucleus, an *elastic nuclear reaction* can occur, in which the repulsion between the two particles is stronger because the nuclear force is stronger than the Coulomb force for ions in close proximity. Thus, in both elastic nuclear reactions and in coulomb scattering events the final particles have

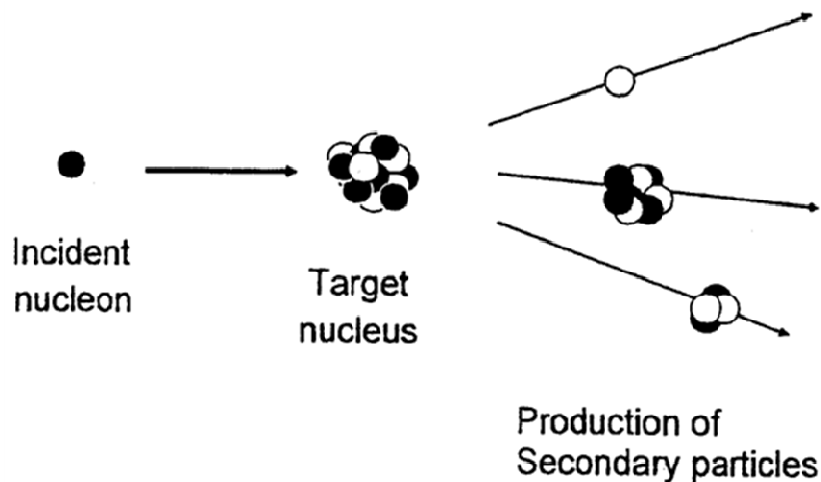

Figure 1: Representation of an inelastic nuclear reaction.

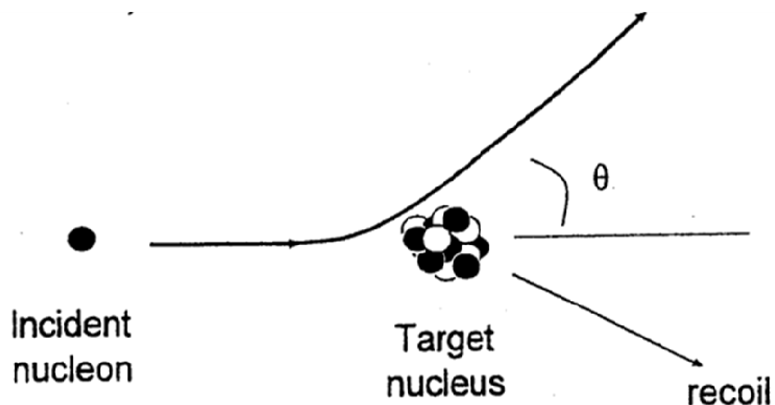

Figure 2: Representation of either a coulomb scattering event, or of an elastic nuclear reaction.

the same mass and atomic numbers as the original particles; only the trajectories and the kinetic energies of the particles change. These two types of reactions are represented by Figure 2. From a SEE point of view, inelastic nuclear reactions tend to be the most significant indirect ionization mechanism, because they tend to have the highest probability of depositing a large amount of charge in the sensitive regions of an IC. Throughout this thesis, the term *nuclear reactions* is used in reference to inelastic nuclear reactions.

Nuclear Reaction-Induced Single Event Effects

Any process that occurs in a semiconductor device as a result of a single particle strike can be called a single event effect. Charge is generated in the device as a result of the particle strike, and that charge can lead to many types of undesirable device behavior. SEEs that cause physical damage to the device are called hard errors. Examples include single event latchup (SEL), single event gate rupture (SEGR), and single event burnout (SEB). SEEs that cause temporary interruption of device performance are called soft errors. Single event transients (SETs), single event upsets (SEUs), and single event functional interrupts (SEFIs) are examples of soft errors.

SEE engineers have typically focused on charge deposition from direct ionization rather than from nuclear reactions when evaluating device reliability in heavy ion environments. For devices with a low critical charge—the charge needed to induce an error on a given circuit node—this focus is warranted, because the error rate will be dominated by direct ionization if the critical charge (Q_{crit}) is sufficiently low. However, devices with a large critical charge may be invulnerable to upsets from direct ionization, leaving nuclear reaction events to dominate the error rate.

Figure 3 was taken from [3] and shows a simulated charge deposition spectrum for 523 MeV ^{20}Ne in the sensitive volume of a certain silicon structure. The details of the structure and of the simulation can be found in [3]. This spectrum is presented as an example to show that, although nuclear reactions are rare when compared with direct ionization (labeled "Electronic Only") events, they can deposit far more charge than direct ionization events.

Figure 4 shows the same results as Figure 3 in integral cross section form. An *integral cross section* corresponds to the probability that the deposited charge **exceeds** the value shown on the x-axis. An integral cross section curve, like that shown in Figure 4, can be produced from a raw counts differential spectrum, like that shown in Figure 3, by using Equation 1, where A_t is the

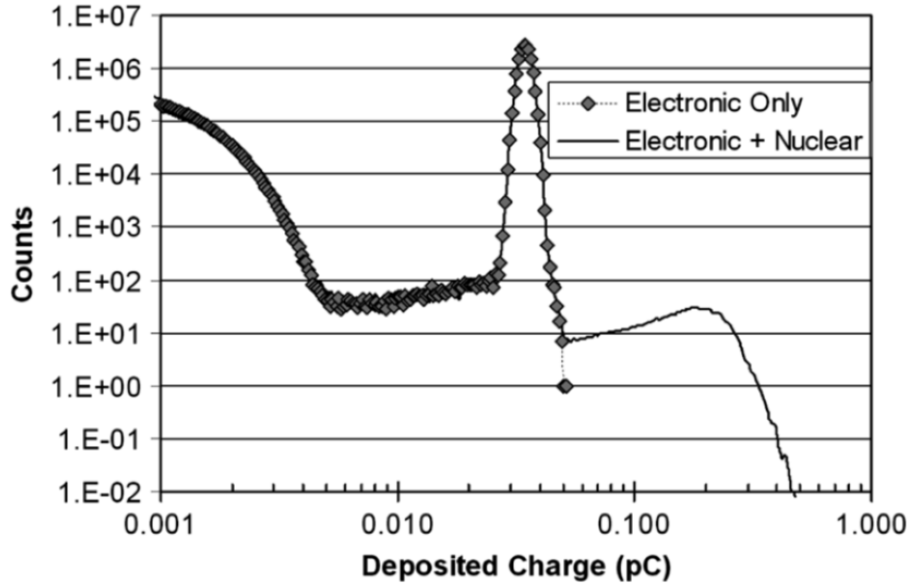

Figure 3: Simulated spectrum of charge deposition from 523 MeV ^{20}Ne in the sensitive volume of a certain silicon structure. Rare nuclear events are capable of depositing large amounts of charge. Taken from [3].

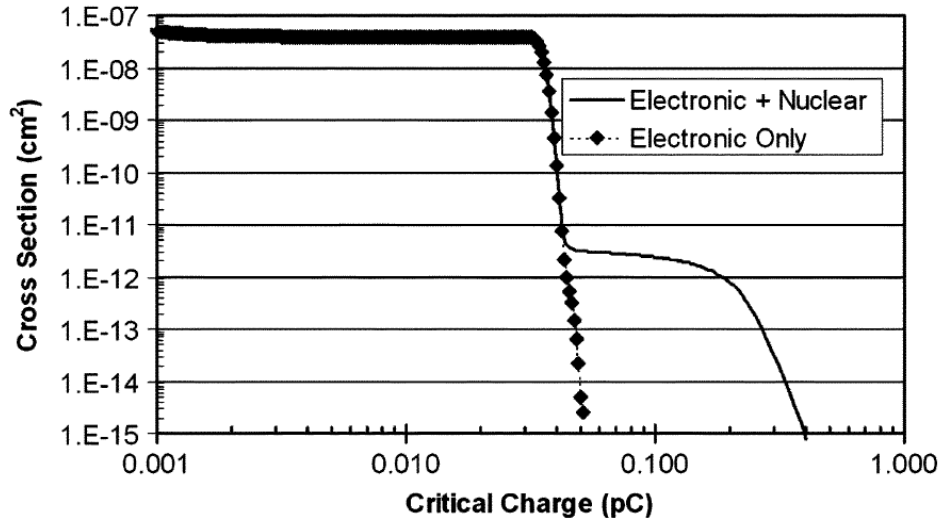

Figure 4: Simulated integral cross section of charge deposition from 523 MeV ^{20}Ne in the sensitive volume of a certain silicon structure. If the critical charge is known then the SEE cross section can be read directly from the curve. Taken from [3].

Equation 1:

$$\sigma(Q_{\text{crit}}) = \frac{A_t}{T} \sum_{i=i(Q_{\text{crit}})}^{\infty} N_i$$

area of the device, T is the total number of particles that struck the device, and N_i is the number of events in the ith bin of the raw spectrum [3]. Note that A_t/T is equivalent to 1/Fluence.

Once an integral cross section is plotted, if the critical charge is known, then the SEE cross section for that type of error can be read directly from the graph. Thus, if the device in Figure 4 had a single event upset (SEU) Q_{crit} of 100 fC then the SEU cross section would be 2×10^{-12} cm^2, but if it had a 10 fC Q_{crit} then the SEU cross section would be 4×10^{-8} cm^2. Figure 4 also demonstrates that nuclear reactions would dominate the error rate for the higher Q_{crit}, whereas direction ionization would dominate the error rate for the lower Q_{crit}.

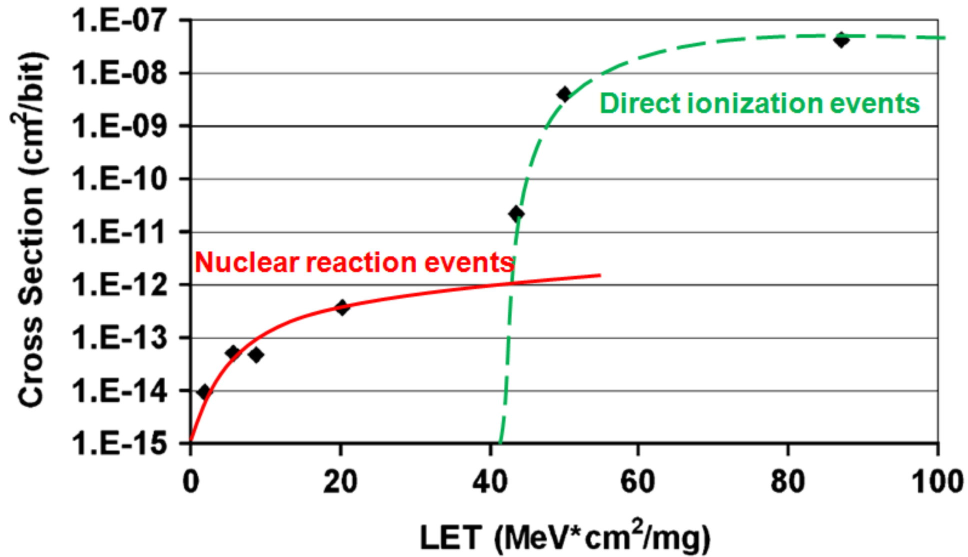

Figure 5: Measured SEU cross section for a radiation-hardened SRAM. Nuclear reactions caused upsets at LET values well below the 40 MeV·cm^2/mg SEU LET threshold of the device. Taken from [3].

Figure 5 [3] shows the measured SEU cross section of a radiation-hardened 4 Mbit SRAM. The cross section is saturated for very high LET values and drops off sharply below the LET threshold of 40 MeV·cm^2/mg. This portion of the data can be predicted reasonably well using the conventional rectangular parallelepided (RPP) technique. In this technique, the average LET of the incident particle is multiplied by the path length of that particle through the sensitive

volume to solve for the amount of charge deposited. If this charge exceeds Q_{crit} then it is predicted that an upset will occur. However, Figure 5 also shows SEUs at very low LET values. These upsets cannot be predicted using the RPP model. The author of [3] performed energy deposition simulations, and was able to predict the cross sections of these upsets reasonably well when accounting for inelastic nuclear reactions. Therefore, the author of [3] concluded that these upsets were likely caused by nuclear reactions. Thus, through nuclear reactions, even devices with a high SEU LET threshold can be upset in a low-LET environment.

Even in devices with a low critical charge, the effects of nuclear reactions can be significant. Although direct ionization may dominate the single bit upset response of a low-Q_{crit} device, nuclear reactions may dominate the multiple bit upset response, the single event functional interrupt response, the single event latchup response, etc. [1]. In addition, all neutron induced SEEs, and nearly all proton induced SEEs, occur through nuclear reactions.

Experiments have been performed with various energies of ions having the same LET in order to attribute observed SEEs to nuclear reactions [1,6]. The premise of these experiments is that, if direct ionization were the dominant error-inducing mechanism, then ions of the same LET would produce the same error rate. The results of such an experiment are shown in Figure 6, which was taken from [6]. The high energy test results in Figure 6, plotted as triangles, show a much higher cross section for SEUs than the low energy test results, which are plotted as circles. This disparity suggests that an energy-dependent charge deposition mechanism is responsible for the observed SEUs. The authors of [1,6] used theory and simulations to attribute these SEUs to inelastic nuclear reactions.

Because of the complex physics involved, nuclear reaction-induced SEE rate prediction must be done with high fidelity simulations. It is important to account for the composition and placement of all materials in or near the sensitive volumes of the device. In particular, the

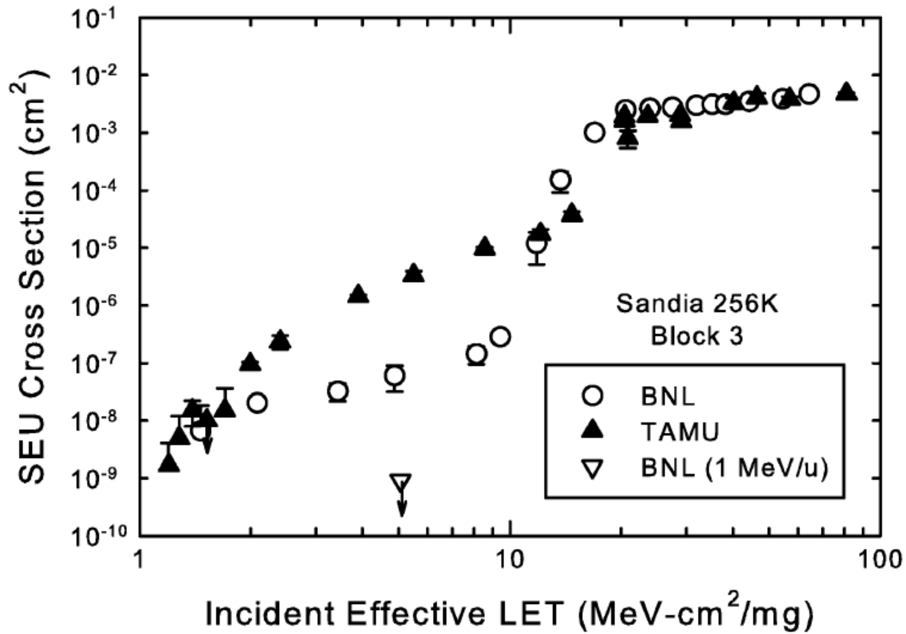

Figure 6: Measured SEU cross section for an SRAM. Even when testing at the same LET value, higher energy ions produce higher SEU cross sections than low energy ions. Taken from [6].

deleterious role of high-Z materials in the IC BEOL has been shown through simulations in [1-5]. High-Z materials can produce high-Z secondary particles, which can be very ionizing. Care must also be taken to accurately model the radiation environment, using the appropriate ion species, energies, and angles. To capture the device response, one must have proper definitions of sensitive volume geometries as well as the charge collection efficiencies and critical charges for those volumes. The fidelity of the nuclear fragmentation code used will have a strong impact on the accuracy of the error rate prediction [1,8]. In short, nuclear reaction-induced SEE rate prediction is a complex problem that requires extensive modifications to existing rate prediction techniques. Proposed modifications are given in [3]. Out of necessity, hardness assurance techniques are also being revisited to account for nuclear reactions [1,6,9].

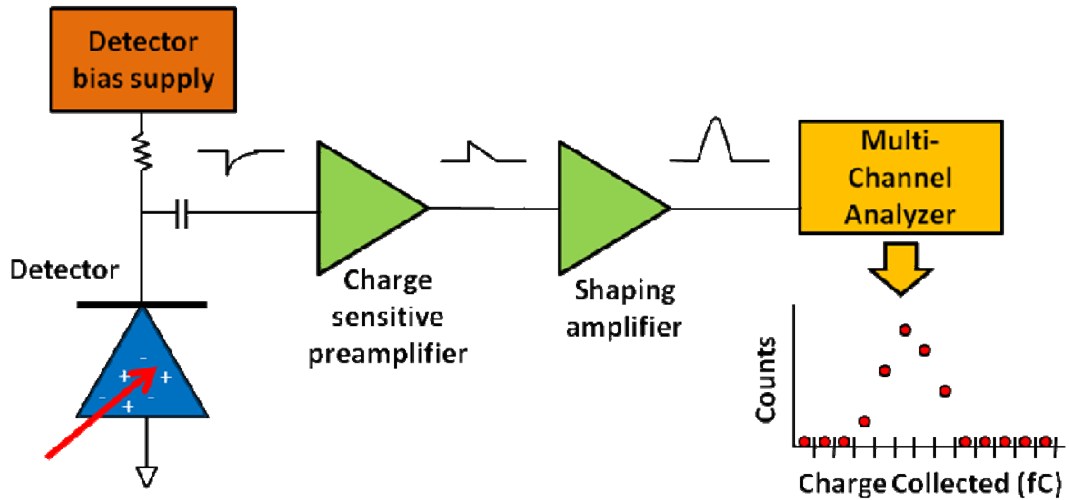

Figure 7: Block diagram of a generic pulse height analysis system. This system can be used to produce a spectrum that characterizes charge generation events in the detector.

Pulse Height Analysis

All of the charge collection measurements in this work were taken using pulse height analysis (PHA) [7]. A block diagram describing PHA is given in Figure 7. To perform PHA, a semiconductor detector is reverse biased in order to ensure that nearly 100% of the charge generated in the detector will be swept to the contacts by the applied electric field. When ionizing radiation strikes the detector a current pulse is then induced, and applied to the input of a *charge sensitive preamplifier*. The preamplifier integrates current over time; therefore, it outputs a pulse whose height is a measure of the amount of charge collected from the detector. This pulse is then amplified and manipulated to have a nearly Gaussian shape by the *shaping amplifier*. This shaped pulse is passed to the *multichannel analyzer*, which digitizes the pulse and histograms it according to its height. This process is repeated for every event that generates charge in the detector, and ultimately produces a differential pulse height spectrum.

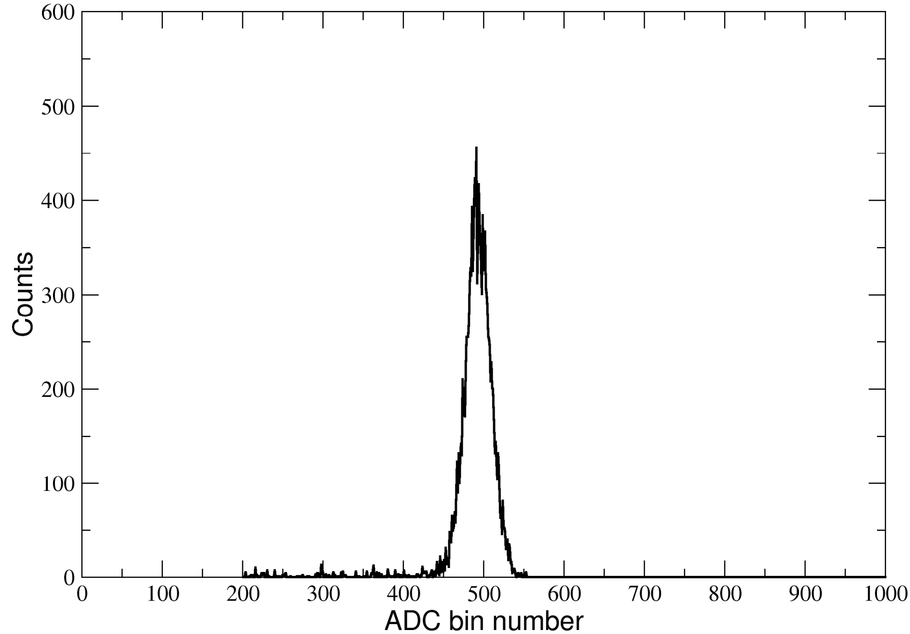

Figure 8: Measured pulse height spectrum from 5.4 MeV alpha particles incident on a silicon surface barrier detector. This spectrum is used to perform an energy calibration by defining the centroid of the distribution, bin number 495, to occur at 5.4 MeV.

By calibrating the PHA system, the differential pulse height spectrum can be read directly in terms of charge collection. Thus, a calibrated PHA system can produce a spectrum like the one shown in Figure 3. The PHA system used in this work was calibrated using a Polonium-210 radioactive source that emits 5.4 MeV alpha particles. The alpha particles were stopped in a reverse-biased silicon surface barrier detector (SBD), and therefore deposited their total energy. Energy deposited in silicon generates charge with a conversion factor of 22.5 keV/fC [10]. Thus, the amount of charge generation is readily known, and because the SBD has near 100% charge collection efficiency, this is the amount of charge that is injected into the preamplifier of the PHA system as a current pulse. These alpha-induced current pulses are processed and digitized to produce a roughly Gaussian distribution of pulse height events, as shown in Figure 8. The centroid of this distribution is defined to occur at the energy of the incident alpha particles—5.4 MeV. This provides one energy calibration point. A second point is obtained by assuming

that the 0th bin of the analog-to-digital converter (ADC) corresponds to 0 MeV. Because the PHA system is highly linear, these two calibration points allow us to interpret all of the 4096 bins of the ADC in terms of energy deposited. Although this crude calibration method would be inadequate for some applications (e.g., alpha spectroscopy) it is sufficient for the purposes of this study.

CHAPTER III

EXPERIMENTAL DESIGN

Observability of Nuclear Events

Modern ICs are often composed of millions of devices, and can therefore contain millions of sensitive volumes. Because of the large number of sensitive volumes, even rare nuclear reaction events like those shown in Figure 4 can, at times, be readily observed as a deviation from normal device functionality. One goal of this study is to measure the charge collected from these rare nuclear reactions events. However, it would be impractical to simultaneously perform PHA on millions of sensitive devices. The PHA system chosen for this study is capable of simultaneous charge collection measurements from 16 detectors, allowing for some parallelization of data acquisition during broadbeam testing. In order to further increase the observability of nuclear reaction events, the test structures used in this study have a much larger sensitive volume area than one would find in a realistic IC device. The test structures are described in the next section.

It was necessary to irradiate the test structures to a minimum fluence of 10^9 cm^{-2} in order to observe a statistically significant number of rare nuclear events. This high fluence can only be achieved in a reasonable amount of time by using a high beam flux. There is a limit to the rate at which a PHA system can process charge collection events. When that rate is exceeded then many charge deposition events can be missed, because they occur while the PHA system is busy processing previous events. The percentage of the time that the PHA system is busy is called the *dead time*. The dead time was measured and kept low by limiting the flux, and by designing a high-bandwidth PHA system.

Pileup is another testing difficulty that must be considered for when performing PHA on large area devices with a high beam flux. *Pileup* occurs when two (or more) incident particles strike the detector at virtually the same time. The PHA system cannot distinguish these as separate charge deposition events, so an artificially-high charge collection event is recorded. Poisson statistics can be used to calculate the probability of an n-fold pileup event, as shown in Equation 2 [7]. This equation gives the probability for observing exactly n events, when the expected number of events in the time interval is λ. For the purpose of predicting pileup in a PHA system, λ can be calculated by multiplying the beam flux by the sensitive area of the detector and by the shaping time constant used in the shaping amplifier.

Equation 2:

$$P(n, \lambda) = \frac{\lambda^n e^{-\lambda}}{n!}$$

These pileup events can have a higher cross section than nuclear events, and therefore overwhelm the nuclear events in their respective region of the pulse height spectrum. The interference of pileup events with the nuclear events being studied was minimized by testing with low LET ions incident on a relatively thin sensitive volume. These two conditions ensured that very little charge was generated due to direct ionization, and therefore even when pileup occurs they affect such low ADC bin numbers that the observability of nuclear events is not reduced. The lower level discriminator of the PHA system was set in order to cut off these direct ionization events, which also significantly reduced the system dead time.

High LET beam contaminants were also encountered, and are described in Chapter IV. These events are similar to pileup in that they can overwhelm the nuclear events in a certain region of the pulse height spectrum. These events have been identified in the spectra presented in this work. No effort was made to reduce beam contamination levels because this mechanism was identified late in the study.

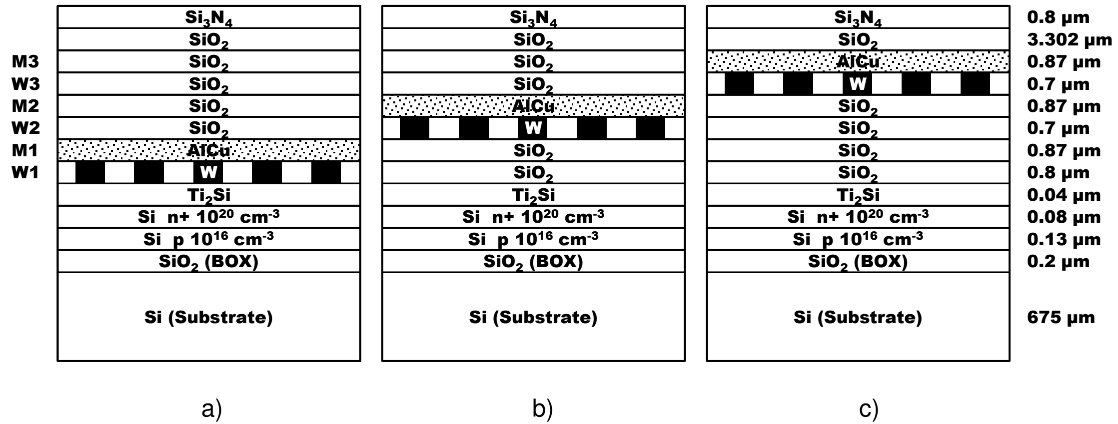

Figure 9: SOI test structures containing metallization at the (a) W1 and M1 layers, (b) W2 and M2 layers, and (c) W3 and M3 layers. These and other test structures allow identification of the role of overlayer materials on charge generation in the active silicon. Not drawn to scale.

Test Structures

Sandia National Laboratories fabricated SOI vertical n+/p diodes for this study with their CMOS7 technology. The diodes have a large surface area, $307 \times 601\ \mu m^2$, in order to maximize the number of events that can be observed during a reasonable heavy ion exposure. They were overlaid with various materials in order to determine the overlayers' effect on charge collection in the diode. In this paper, the metallization layers are identified with either a "W", for tungsten layers, or with an "M", for the AlCu metal layers, followed by the level number (e.g., W1 is tungsten level 1, meaning the level closest to the silicon).

Several overlayer configurations were fabricated, three of which are shown in Figure 9. The "W1 + M1" configuration is shown in Figure 9(a). Looking up from the charge collection region (i.e., the silicon body) it contains a thin sheet of titanium silicide, 75% tungsten coverage in the W1 layer, a sheet of AlCu at the M1 layer (actual composition, from bottom to top: Ti 0.02 µm /TiN 0.05 µm /AlCu 0.7 µm /TiN 0.1 µm), and 100% oxide on all other process metallization layers. Figure 9(b) shows the "W2 + M2" configuration, which is the same structure except that the W and AlCu are one level higher. These materials are raised an

additional level in the "W3 + M3" configuration, shown in Figure 9(c). The "M1" structure (not shown) only has AlCu at level 1. The final structure used in this study (not shown in figure) is called "Oxide Only". It contains no W or AlCu.

These test structures allow us to isolate and identify the contributions of the W and AlCu layers to charge collection in the underlying silicon body. Note that 75% W coverage and 100% AlCu coverage is far more metallization than is used in typical IC devices. This was done to make the effects of the metallization on charge collection more observable. For all tests the diodes were reverse biased with 3 V and the substrate was grounded.

The diodes were fabricated in a SOI technology with the intent of having well-defined sensitive volumes. One must have clearly defined sensitive volumes to be able to quantitatively compare experimental data with energy deposition simulation results. With SOI devices, typically charge is collected only from the silicon body; the buried oxide prevents any charge from being collected from the substrate. However, high LET heavy ion tests (ranging from 10 – 60 MeV·cm^2/mg) revealed that the sensitive volume thickness of these diodes extends as deep as several microns into the substrate. Testing further revealed that the sensitive volume thickness of the diodes is not constant for various LET values, although charge collection does increase monotonically as LET is increased. Finally, testing revealed that coincident charge collection events often occur in separate diodes, but only for diodes located on the same die. These complex charge collection mechanisms in the diodes were identified as being caused by displacement currents. These test structures are very similar to those used in [11,12] for studying displacement currents in that they have a large area, low substrate doping, and a relatively thin buried oxide (200 nm). Unfortunately, these are also the conditions under which displacement current becomes significant. This complex charge collection mechanism occurs because the electric field from the reverse biased diode in the silicon body penetrates some distance into the substrate. This electric field separates the charges that are generated in the substrate, and causes

charge of a certain polarity to accumulate beneath the buried oxide. This charge is mirrored in the silicon body because the silicon body and the substrate act as the plates of a capacitor. This charge is then collected by the PHA system. In [11,12] it was shown that this mechanism could cause charge sharing between devices separated by hundreds of microns of SiO_2, as was the case here. Despite this complex charge collection mechanism, data from these test structures are still useful because they can be used to show **differences** in charge collection between diodes having different overlayer configurations. However, this mechanism prevents us from being able to quantitatively compare experimental data with energy deposition simulation results.

Test Setup

A block diagram of the test configuration is given in Figure 10. The 16-channel PHA system designed for this study relies on the Mesytec MPRS-16 preamplifier/shaping amplifier, used in conjunction with the Phillips Scientific 7164H peak sensing ADC. The 7164H is a module following the Computer Automated Measurement And Control (CAMAC) standard, so a CAMAC crate controller is needed to interface with it. The Kinetic Systems 3988 General Purpose Interface Bus (GPIB) crate controller was used. In order to prevent the long latency of the GPIB standard from reducing the PHA system's bandwidth, a HYTEC 1342 auxiliary crate controller was used in List Mode. The 1342 stored the PHA events in a buffer, which was periodically read out by the 3988. The software controlling it all was written by Marcus Mendenhall using the Python Laboratory Operations Toolkit [13]. This software saves every digitization event with a timestamp, allowing for great flexibility when postprocessing data.

A discriminator board was designed and built as a custom printed circuit board (PCB), in order to detect when a shaped pulse from the Mesytec exceeded some threshold voltage, and then to trigger the Phillips Scientific 7164H to digitize that pulse. The design of the discriminator

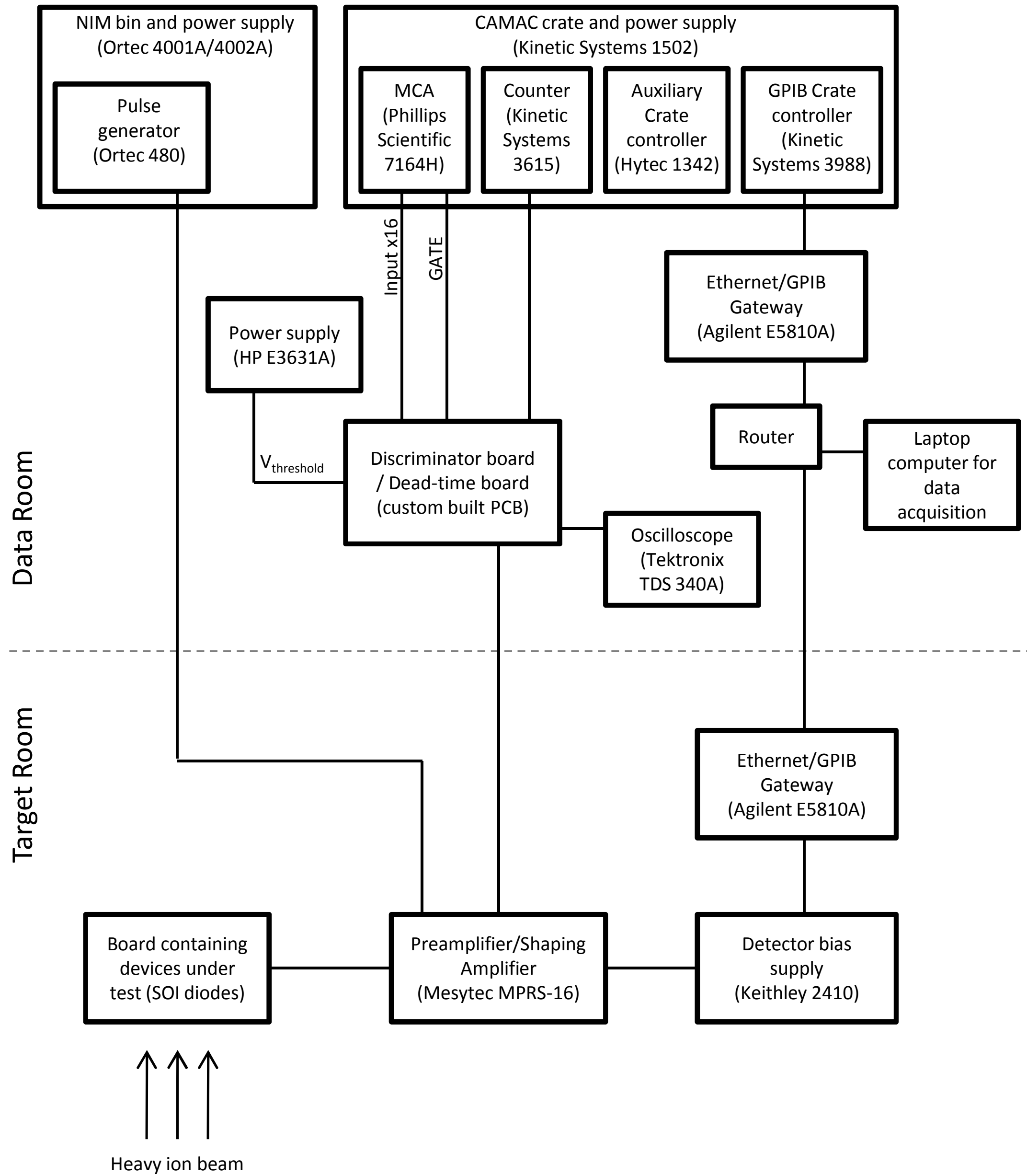

Figure 10: Block diagram of the 16-channel PHA system and auxiliary equipment.

board is given in Appendix A. Note that, once triggered, the 7164H digitizes the signals present at that moment **on all 16 inputs**. This increases the dead time of the PHA system. However, it also allowed for the identification of anomalous events that were manifest as large-amplitude

charge collection events affecting multiple channels at the same time. One such type of anomalous event is shown in Figure 11(a). These events were identified as being caused by noise spikes on the detector bias supply power line (see Figure 7). These events were removed from the pulse height spectra through postprocessing, as is shown in Figure 11(b). As mentioned in the Test Structures section, another such type of anomalous event was identified as being caused by displacement currents in the test structures, which caused charge sharing between diodes on the same die. These coincident events were also removed through postprocessing.

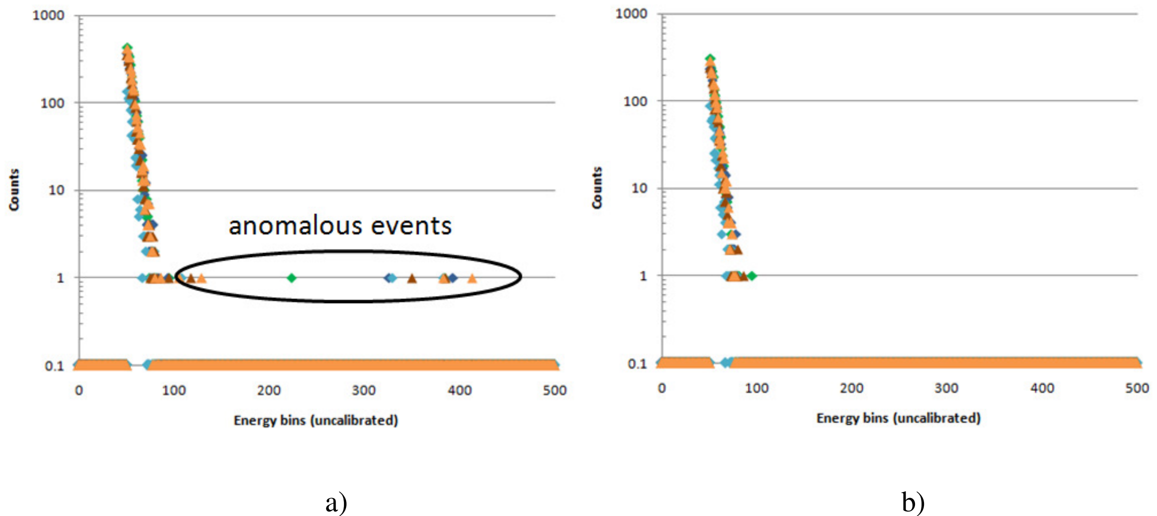

Figure 11: A noise spike on the detector bias supply line caused the anomalous large-amplitude events shown in (a). These events affect multiple channels in the same digitization cycle, and were filtered from the data via post-processing, as shown in (b).

The dead time of the system was measured by sampling the BUSY signal of the 7164H at 10 MHz. The fraction of the time that BUSY was asserted was defined as the dead time, and was determined using the Kinetic Systems 3615 Counter.

Displacement damage in the diodes was observed following certain high-fluence heavy ion tests, particularly when testing with lower energy incident particles. This damage causes a

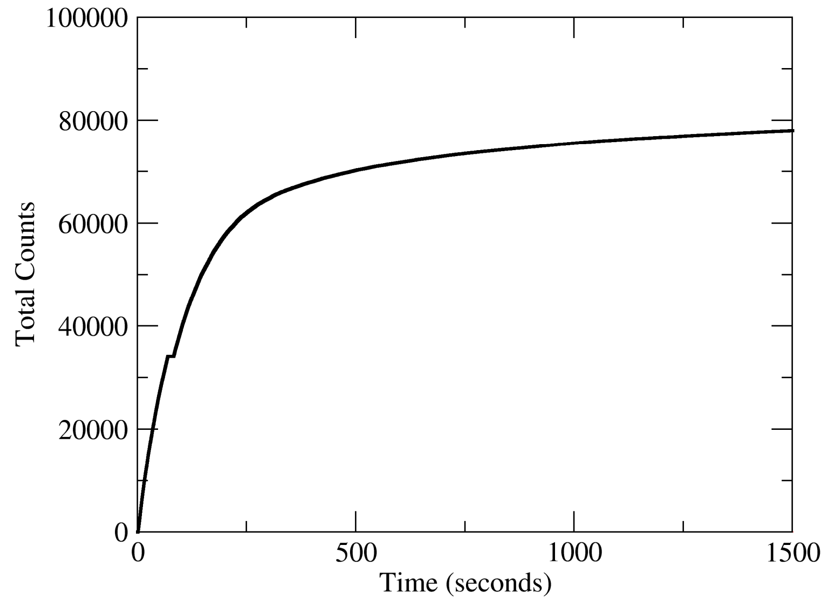

Figure 12: Measurement of the total number of counts during a high fluence heavy ion exposure. This non-linear curve shows that the count rate was decreasing over time, because of displacement damage in the diodes.

decrease in the charge collection efficiency of the diodes; therefore, its occurrence must be identified so that the damaged diodes can be replaced with new ones. The proper functionality of the diodes was monitored by continuously measuring the leakage currents of the diodes by using a Keithley 2410 as the detector bias supply. Displacement damage in the diode is accompanied by a significant increase in leakage current. Displacement damage was also detected by observing that the count rate of the PHA system steadily decreased, even though the beam flux was constant. Figure 12 shows how the total number of counts increased while the diodes were irradiated with 10 MeV/u oxygen to a fluence of 2×10^{10} cm^{-2}. If the count rate were constant over time then Figure 12 would show a straight line. Instead, the count rate is seen to steadily decrease, due to the reduced charge collection efficiency of the damaged diodes.

An oscilloscope was used throughout the experiments to view the unipolar pulses that were being digitized. An oscilloscope is useful to identify noise sources so that they can be

eliminated, and so that the experimenter will know if the unipolar pulses being digitized are ill-formed or saturated.

Heavy Ion Irradiation

Heavy ion irradiations were performed at three facilities providing different energies: 16 MeV/u at Lawrence Berkeley National Laboratory (LBNL), 40 MeV/u at Texas A&M University (TAMU), and 1000 MeV/u at the NASA Space Radiation Laboratory (NSRL). NSRL is located at Brookhaven National Laboratory, and is a unique facility that is not typically used for SEE testing. Table 1 lists the heavy ions used.

TABLE I
HEAVY ION BEAMS USED IN THIS WORK

Energy (MeV/u)	Ion	LET (MeV·cm^2/mg)	Facility
16	Nitrogen	1.2	LBNL
40	Neon	1.2	TAMU
1000	Iron	1.2	NSRL

All of the ions used have an LET of 1.2 MeV·cm^2/mg. These ions have a long range compared to the thickness of the overlayer materials of the test structures, so this is essentially the LET that affects the sensitive volume. This relatively low LET value was chosen in order to reduce the contribution of direct ionization to the measurements, making indirect ionization events more observable. Because a constant LET was used, any differences in device response could be attributed to indirect ionization mechanisms.

Figure 13 shows that the LET of a heavy ion beam can be held constant while increasing particle energy by increasing the atomic number of the ions in the beam. Note that LET has a complex dependence on energy when the full energy spectrum is considered. A discussion of the

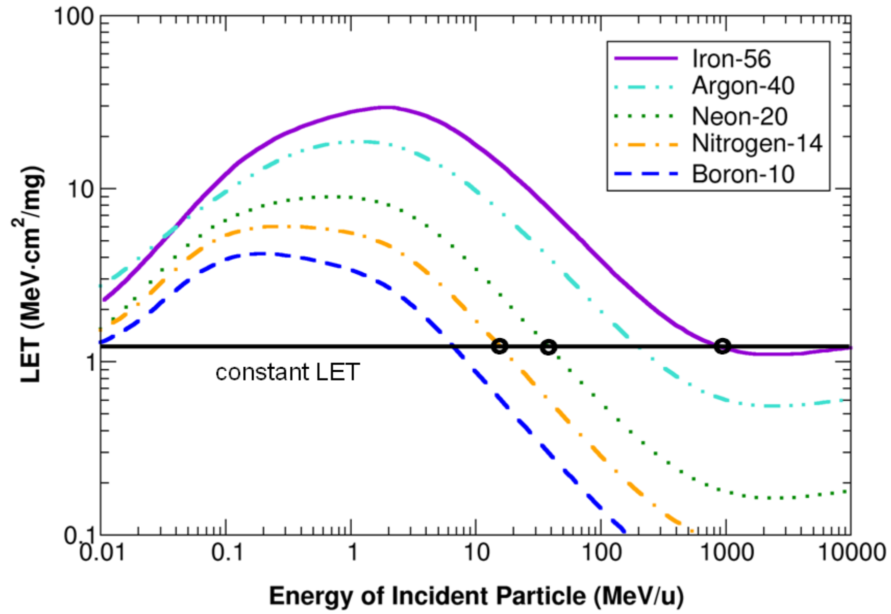

Figure 13: LET can be held constant while increasing particle energy by increasing the atomic number of the ions in the beam. Circles represent the heavy ion beams used in this work. Generated using SRIM-2008 [15].

physics of energy loss can be found in [14]. SEE testing is typically performed at energies between a few MeV/u and 1000 MeV/u. Within this energy range, the same LET can be obtained using a variety of ions at the appropriate energies.

CHAPTER IV

IMPACT OF THE PRESENCE AND PLACEMENT OF TUNGSTEN

The results of 40 MeV/u ^{20}Ne tests are shown in integral cross section form in Figure 14. The W1 + M1 structure exhibited the most extreme charge collection events; as much as 530 fC was collected. This clearly shows that, for this structure, the most charge collection occurs when tungsten is present and is closest to the active silicon. Fewer extreme events were observed in the W2 + M2 structure, and a statistically insignificant number of extreme events were observed in the W3 + M3 structure.

It is not surprising that the most extreme charge collection events were observed when tungsten was closest to the active silicon. Nuclear reactions occurring in the lower levels can

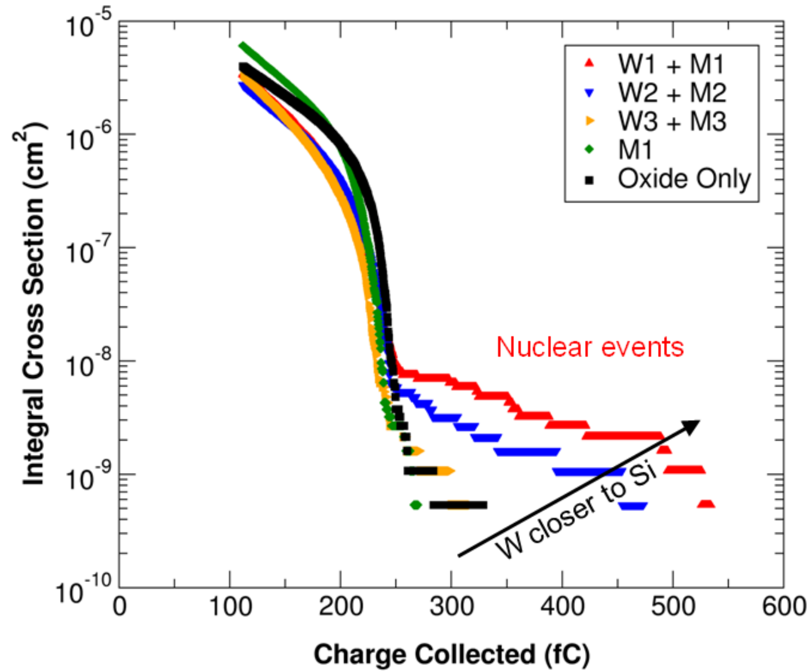

Figure 14: Measured integral cross section of 40 MeV/u ^{20}Ne ions on the test structures. The presence of tungsten near the active silicon led to extreme charge collection events.

more easily eject secondary particles at high angles through the sensitive volume, allowing them to deposit more charge due to their longer path length. Also, secondary particles originating at higher levels may have insufficient range to reach the sensitive volume. Finally, secondary particles originating at higher levels lose energy as they penetrate the lower levels. If a secondary particle has an initial energy corresponding to the Bragg peak energy for that ion (see the function maxima in Figure 13) then the loss of energy in overlayers would make the particle less ionizing. However, if its initial energy is greater than the Bragg peak energy, it can be seen in Figure 13 that the loss of energy in overlayers could make the particle more ionizing. Therefore, under certain conditions, it is possible that tungsten further from the sensitive volume could contribute the most to nuclear reaction-induced charge generation.

These findings somewhat differ from those given in [5], in which simulation results for a certain device showed little charge generation dependence on the vertical position of the tungsten plugs, but a strong dependence on the lateral position of the tungsten plugs relative to the sensitive volume. However, the structure simulated in [5] had a smaller sensitive volume that was laterally offset from the overlying tungsten plugs (corresponding to the layout of an actual SRAM cell), and, as the author noted, the angular distribution of the secondary particles affected the outcome of the study. Therefore, when considered together, Figure 14 and the work of [5] strongly suggest that nuclear reaction-induced charge generation is a function of the vertical and lateral position of the tungsten relative to the sensitive volume, as well as the nuclear breakup pattern.

No statistical difference can be seen between the responses of the M1 and Oxide Only structures in Figure 14, meaning the Ti/TiN/AlCu/TiN metal layer did not cause any more large-amplitude events than similarly placed SiO_2 layers. This meets expectations because the fraction of the M1 layer filled by Ti or Cu is too small to significantly affect the cross sections, and the lower-Z Al and N atoms will have the same effect as oxide because they can only produce low-Z

secondary particles, which therefore have low LET. These results show that high-Z materials have a greater impact on nuclear reaction-induced charge collection than low-Z materials.

No events are shown in Figure 14 below 120 fC because that is where the discriminator was set during heavy ion irradiation. This was done to keep the count rate low so that dead time losses in the PHA system would not reduce the observability of extreme charge collection events. Direct ionization events caused by 40 MeV/u ^{20}Ne are not shown because they fall beneath this threshold, however they have an integral cross section value of 1.8×10^{-3} cm^2 (the diode area). The events below 250 fC are likely caused by direct ionization from beam contaminants (i.e., ions in the beam other than ^{20}Ne). Because of this finding it is recommended that studies focused on low cross section events (e.g., nuclear reactions) should first characterize the beam's purity, and, when possible, purge high-LET contaminants from the beam. The events beyond 250 fC are clearly caused by nuclear reactions because their cross sections are several orders of magnitude below the ^{20}Ne direct ionization events. Despite their rarity, these extreme charge collection events can dominate the error rate in devices with a high critical charge [1-3].

CHAPTER V

IMPACT OF ION ENERGY ON CHARGE COLLECTION

Data on Ion Energy Dependence

Figure 15 was taken from [6], and shows that SEU cross sections for the SRAM studied increase as incident particle energy increases and LET is held constant. However, data are only given up to 40 MeV/u, and the author questioned whether these SEU cross sections increase without bound as primary particle energy increases [6]. Such an increasing trend could lead to the vast underprediction of on-orbit error rates, because heavy ions exist in the space environment that are far more energetic than those typically used in ground facilities for hardness assurance testing. Figure 16 was taken from [16], and shows the differential energy spectra of a few prominent ions in the GCR spectrum. As seen in Figure 16, the differential flux peak of GCR ions is approximately 500 MeV/u. However, the median differential flux is approximately 1500 MeV/u, so half of all the ions in the GCR spectrum have energies exceeding this value. Thus, GCR energies are orders of magnitude greater than those used for ground based testing, so it is vitally important to understand the effect of ion energy on nuclear reaction induced SEEs.

Tests were performed at NSRL with 1000 MeV/u ^{56}Fe—a prominent and potentially very harmful ion in the GCR spectrum. This ion has the same LET as 40 MeV/u ^{20}Ne: 1.2 MeV·cm^2/mg. Although 1000 MeV/u ^{56}Fe is a more energetic and heavier ion than 40 MeV/u ^{20}Ne, Figure 17 shows that 40 MeV/u ^{20}Ne resulted in larger-amplitude charge collection events. With 1000 MeV/u ^{56}Fe, events in the W2 + M2 structure were limited to 115 fC, whereas with 40 MeV/u ^{20}Ne they ranged up to 470 fC. This clearly shows that nuclear reaction-induced

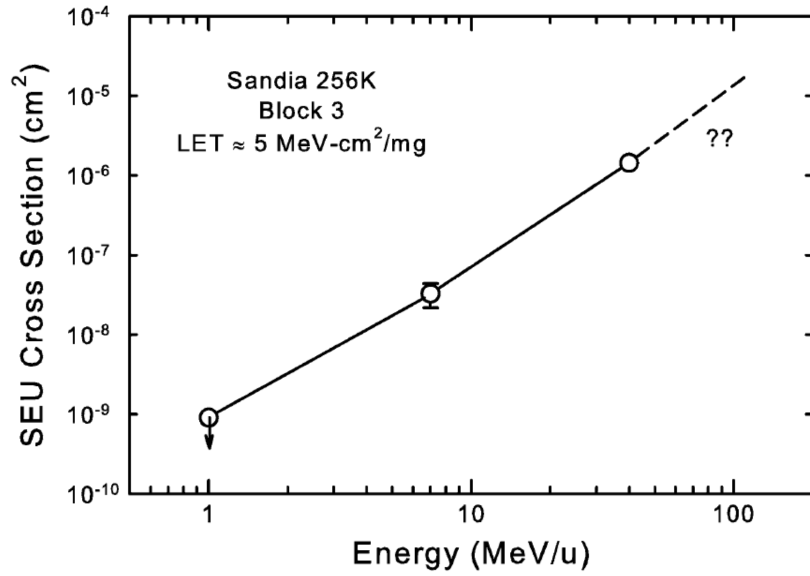

Figure 15: Measured SEU cross section as a function of energy at an incident effective LET of ~5 MeV·cm^2/mg. These data raise the question of whether SEU cross sections increase without bound as particle energy increases and LET is held constant. Taken from [6].

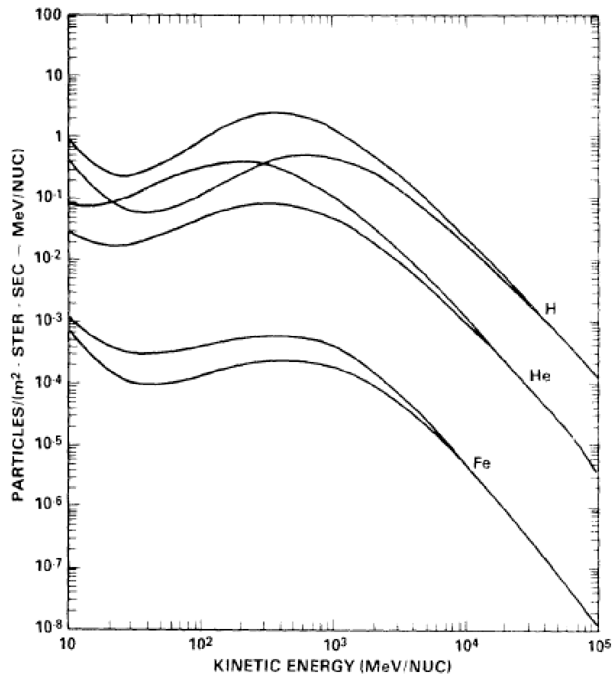

Figure 16: The galactic cosmic ray differential energy spectra for hydrogen, helium, and iron. Taken from [16].

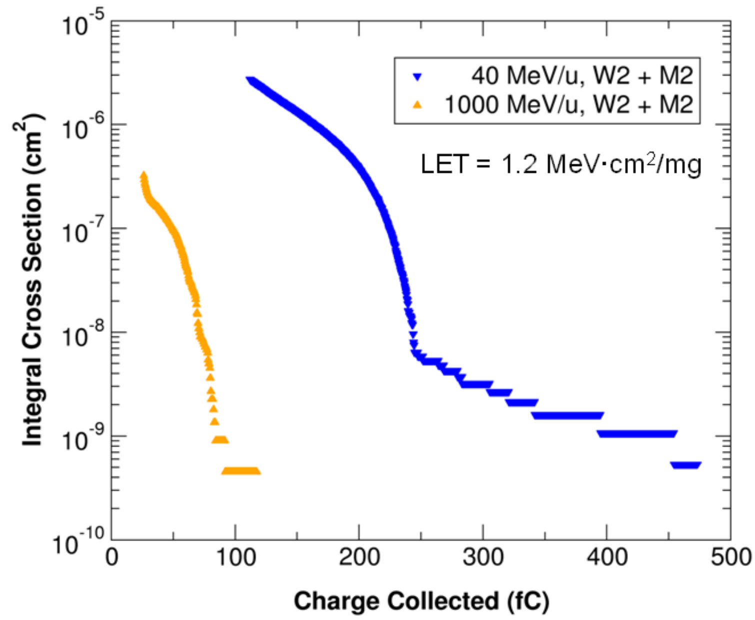

Figure 17: Measured integral cross section from the test structures for two heavy ion beams with the same LET. The higher energy test produced smaller-amplitude charge collection events.

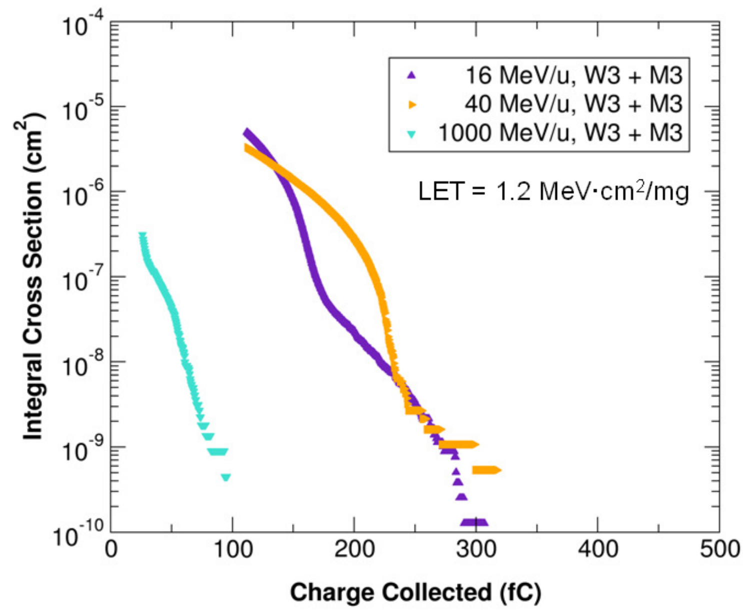

Figure 18: Measured integral cross section from the test structures for three heavy ion beams with the same LET. The higher energy test produced smaller-amplitude charge collection events.

charge collection does not grow without bound as particle energy increases and LET is held constant, and suggests that, beyond a certain energy, it actually decreases. This turning-point energy is therefore the worst-case energy for SEE testing at that LET, and depends on the device layout and technology. The mechanism responsible for the decrease in nuclear reaction-induced charge collection beyond the worst-case energy is explored in the Physical Mechanism section.

Figure 18 shows the integral cross section of heavy ion data on the W3 + M3 test structures at 16 MeV/u, 40 MeV/u, and 1000 MeV/u, all with the same LET. These data are consistent with Figure 15 because 40 MeV/u resulted in a similar response as 16 MeV/u. They are also consistent with Figure 17 because 1000 MeV/u is again seen to result in lower-amplitude charge collection events. This suggests that the worst-case energy for nuclear reaction-induced charge collection exists somewhere between 40 MeV/u and 1000 MeV/u at this LET for these devices.

Simulations Identifying Worst-Case Energy

Previous simulation results for a bulk-Si device showed the impact of 25 MeV/u and 500 MeV/u heavy ions on indirect ionization [2]. These results showed that when tungsten was present in the device, higher-energy testing was needed to produce a conservative estimate of the on-orbit response. However, [2] does not identify the high energy that should be used for SEE testing. In order to identify the worst-case energy for nuclear reaction-induced charge generation, simulations were performed using Monte Carlo Radiative Energy Deposition (MRED) [1-3,5], a Geant4-based radiation transport code developed at Vanderbilt University. MRED version 9.0.0 was used—which relies on Geant4 9.2.p01—with the binary cascade nuclear fragmentation model. MRED was also used to guide the experiments and to provide insight into nuclear interaction mechanisms.

The worst-case energy for nuclear reaction-induced charge generation will depend on the technology, the device layout, and the fixed LET value chosen. The following examples demonstrate the approach to identify the worst-case energies of certain bulk-Si and SOI devices.

The bulk-Si SEU hardened SRAM presented in [3] was simulated in this work. As was done in [3], the metallization was simplified in the simulations as a sheet of tungsten at level 2 and sheets of aluminum at levels 1-3. The sensitive volume is $2 \times 2\ \mu m^2$ laterally and $2.25\ \mu m$ thick. This sensitive volume was placed at the top center of a $50 \times 50 \times 50\ \mu m^3$ substrate so that the simulation would account for secondary particles originating far away from the sensitive volume. MRED was then used to simulate irradiations of the device at normal incidence with various ion energies and species, all having an LET of 1.2 MeV·cm^2/mg. Note that ^{56}Fe has this same LET at 10000 MeV/u and at 1000 MeV/u, as seen in Figure 13. The resulting integral cross section curves of five of the energies simulated are shown in Figure 19.

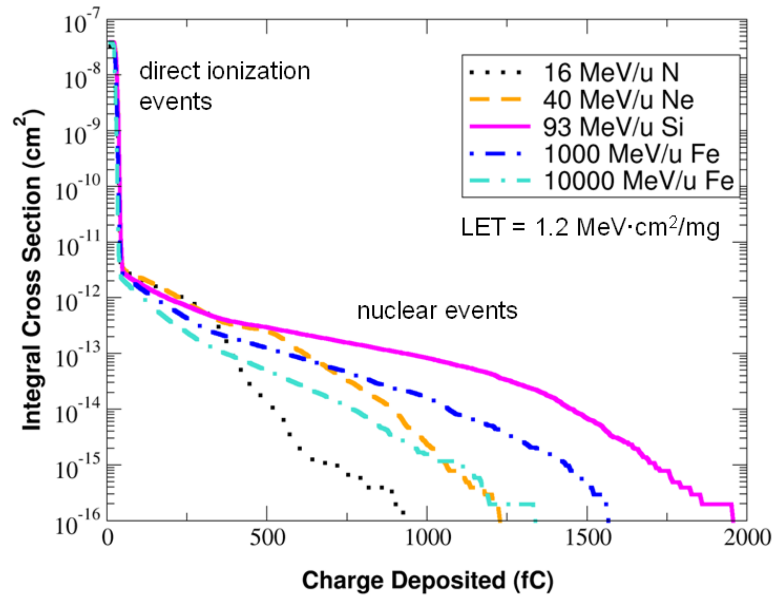

Figure 19: Simulated integral cross section of various fixed-LET heavy ions on a bulk-Si device.

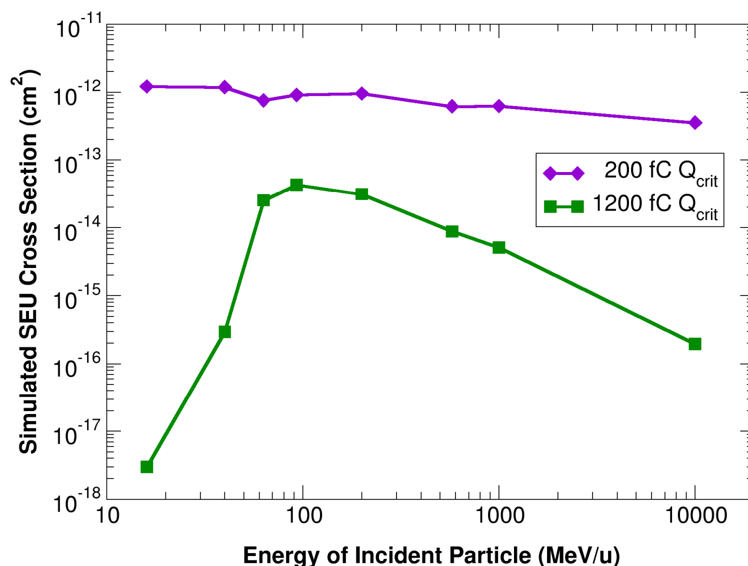

Figure 20: Simulated SEU cross section as a function of energy for a bulk-Si device. The worst-case energy, or the energy resulting in the highest SEU cross section, depends on Q_{crit}.

As seen in Figure 19, if the critical charge to cause an upset is greater than the charge deposited by direct ionization events, then nuclear reaction events will dominate the error rate. The worst-case energy (i.e., the energy producing the highest integral cross section) will depend on the critical charge. In [3], the SEU hardened SRAM cell had a Q_{crit} of 1200 fC. This critical charge was then applied to the integral cross section curves, producing the set in Figure 20 labeled "1200 fC Q_{crit}". Figure 20 shows the simulated SEU cross sections as a function of ion energy for 1.2 MeV·cm^2/mg ions. It can be seen that the worst-case energy for this 1200 fC critical charge device is approximately 100 MeV/u, and that beyond this energy the SEU cross sections decrease. However, if the device had a 200 fC critical charge then the Figure 20 set labeled "200 fC Q_{crit}" would show its SEU energy dependence. This set shows very little dependence on ion energy, and testing at 16 MeV/u would produce a conservative estimate of the on-orbit response for this LET.

Corresponding simulations were performed on the CMOS7 Sandia SOI technology tested in this paper. A sheet of tungsten was again simulated at level 2, and the sensitive volume

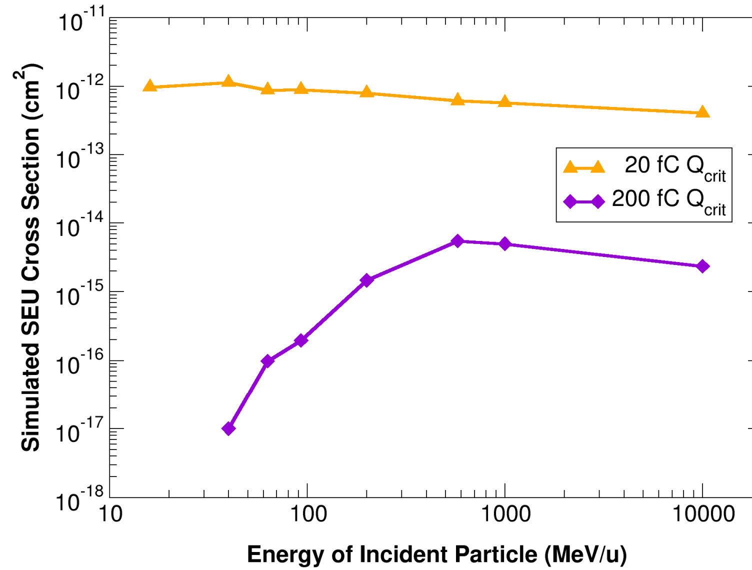

Figure 21: Simulated SEU cross section as a function of energy for an SOI device. The worst-case energy, or the energy resulting in the highest SEU cross section, depends on Q_{crit}.

dimensions used were 2×2 μm^2 laterally and 0.13 μm thick. By producing the integral cross section curves and again choosing a critical charge of 200 fC, the Figure 21 set labeled "200 fC Q_{crit}" was produced. This shows that such a device would have a worst-case energy of about 500 MeV/u for this LET. The worst-case energy is higher for the SOI device than for the bulk-Si device, primarily because the interaction of secondary particles with the SOI device's thinner sensitive volume leads to a different charge deposition response. If the SOI device had a 20 fC critical charge, then the Figure 21 set labeled "20 fC Q_{crit}" would show its SEU energy dependence. As seen in the bulk-Si device, this low Q_{crit} value results in a weak SEU dependence on ion energy, and testing at lower energies would sufficiently estimate the on-orbit response. These results show that the worst-case energy depends not only on the materials surrounding the device, but also on the critical charge and the dimensions of the sensitive volume.

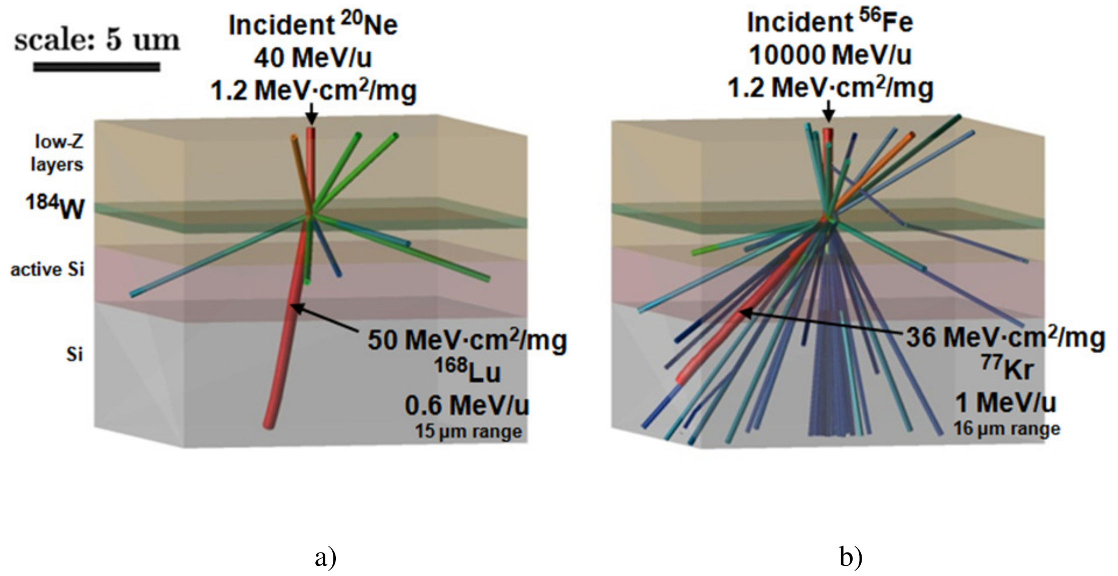

Figure 22: Simulated nuclear spallation reactions caused by a) 40 MeV/u neon and by b) 10000 MeV/u iron. These representative events suggest that very high energy nuclear reactions produce lower-mass and higher-energy secondary particles, which therefore have lower LET.

Physical Mechanism

To identify the mechanism responsible for the decrease in nuclear reaction-induced charge collection beyond the worst-case energy, simulations were performed using the bulk-Si technology described in [3]. Virtual irradiations were performed with 40 MeV/u ^{20}Ne and with 10000 MeV/u ^{56}Fe, both having an LET of 1.2 MeV·cm^2/mg. Events depositing 1200 fC were studied at each energy, providing insight on either end of the spectrum shown in Figure 20. One representative 40 MeV/u event is shown in Figure 22(a) and a representative 10000 MeV/u event is shown in Figure 22(b). Both nuclear events shown occurred in the tungsten layer. Due to the higher incident particle energy and mass, the reaction shown in Figure 22(b) is more violent than the reaction shown in Figure 22(a), as is evidenced by the larger number of resultant secondary particles. Nevertheless, both events deposit 1200 fC in the sensitive volume. Closer inspection reveals that the heaviest secondary particle produced by the 40 MeV/u reaction is more ionizing than that of the 10000 MeV/u reaction; it has an LET of 50 MeV·cm^2/mg as opposed to

36 MeV·cm^2/mg. It is more ionizing because it has a mass of 168 as opposed to 77. These events suggest that secondary particles produced from very high energy nuclear reactions tend to have lower mass and higher energy than those produced by lower-energy reactions, and are therefore less ionizing. This fragmentation trend could explain the measurements in Figures 17 and 18 in which charge collection decreased at higher particle energies, and in Figures 20 and 21 in which simulated SEU cross sections decreased at higher particle energies.

Of course, it would be inappropriate to form any conclusion based on only two nuclear reaction events. Monte Carlo simulations are needed to understand the statistical nature of nuclear fragmentation patterns. Such simulations were performed to test the theory that very high energy incident particles lead to greater decomposition of the incident and target nuclei, resulting in lower mass and higher energy secondary particles that are less ionizing.

Figure 23 shows the simulated isobaric cross section for secondary particles resulting from irradiating ^{184}W with various 1.2 MeV·cm^2/mg ions. This shows the mass distribution of secondary particles for these projectile-target ion pairs. The cross section is given in units of millibarns. One millibarn is equal to 10^{-27} cm^2. The reason the cross section is so low is that the raw number reported by the simulator has been divided not only by the fluence (as is normally done), but also by the number of W atoms in the target material. Thus, the isobaric cross section is proportional to the probability that an incident particle reacts with a single atom of the target material to produce a secondary particle of a given mass.

The 40 MeV/u ^{20}Ne curve in Figure 23 exhibits a peak just below the full mass of the ^{184}W target, which results from reactions in which a few small fragments are removed. This curve also exhibits peak at roughly half the target mass, resulting from fission of the excited W nucleus which most likely arises from very peripheral collisions. The higher energy curves exhibit a broad distribution of secondary masses, because the collisions are sufficiently energetic to remove a large number of fragments from the target nucleus. This supports the theory that

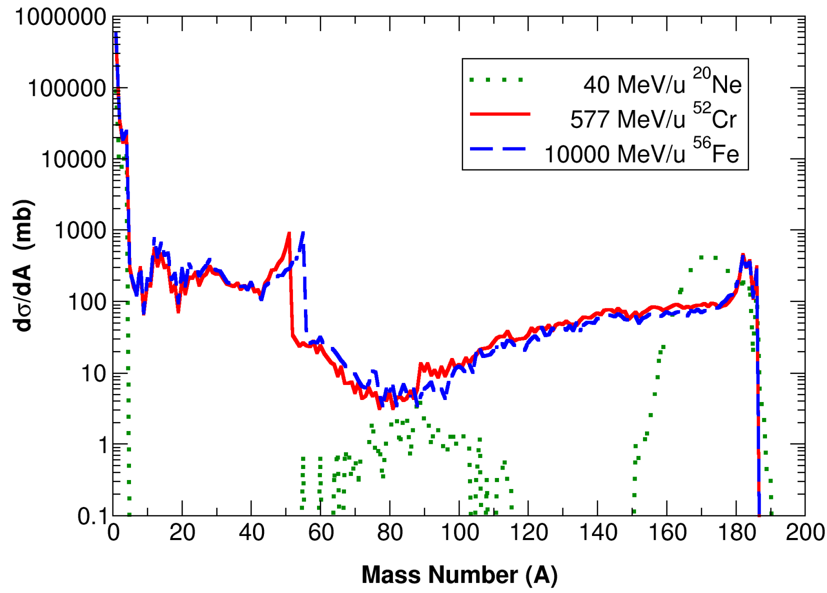

Figure 23: Simulated isobaric cross section for secondary particles resulting from irradiating ^{184}W with various 1.2 MeV·cm^2/mg ions. Results suggest that higher energy incident particles cause greater decomposition of the target nucleus, producing more intermediate and low mass secondary particles.

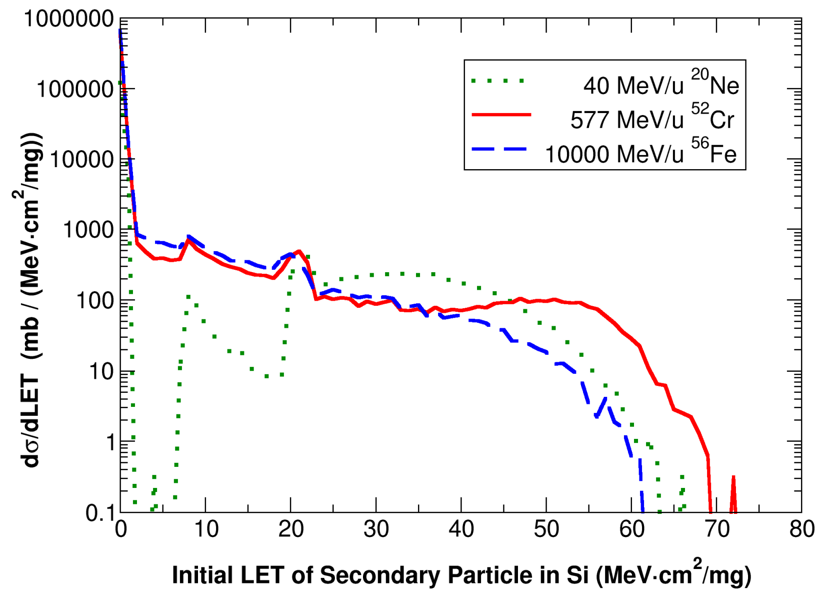

Figure 24: Simulated cross section for the secondary particles produced from various 1.2 MeV·cm2/mg ions incident on ^{184}W as a function of secondary particle initial LET. Results suggest that fewer high LET secondary particles are produced when incident particle energy is increased beyond a certain point.

higher energy incident particles lead to greater decomposition of the target nucleus, resulting in more intermediate and low mass secondary particles. The two higher energy curves are similar because, in both cases, the energy available is far greater than the binding energy of the target nucleus, and because the incident ^{52}Cr and ^{56}Fe ions have similar mass.

These same simulation results are plotted in Figure 24 as the differential of the cross section with respect to the initial LET of the secondary particles in silicon. Values were binned by rounding to the nearest MeV·cm^2/mg. It can be seen that as incident particle energy is increased, while LET is held constant, the production of secondary particles with an initial LET greater than 50 MeV·cm^2/mg first increases and then decreases. This result explains the shapes of the curves in Figures 20 and 21 for devices with a large critical charge. It also strengthens the theory that, as fixed-LET incident particle energy is increased beyond a certain point, the resultant secondary particles will have lower LET. This theory has serious implications for SEE hardened devices flown in the galactic cosmic ray environment and requires further investigation. Such investigation should include the inspection of a broad range of projectile-target ion pairs over a broad range of energies.

Hardness Assurance Implications

If the device to be characterized has a critical charge that is not significantly greater than the charge that could be deposited by direct ionization, then low energy testing will produce a conservative estimate of the on-orbit response, as shown in Figures 20 and 21. However, if the critical charge is many times greater than that which could be deposited by direct ionization then the beam energy used will strongly affect the outcome of the study. Multiple tests over a wide range of energies would assure that the worst-case response is observed. This approach is often impractical due to scheduling pressures and economic reasons. In addition, high energy facilities are generally less accessible. A review of facilities typically used for SEE testing is given in [17].

As an alternative to testing at various energies, the energy producing the worst-case response can be identified through simulations following the approach described in this chapter. The accuracy of this method will depend on the fidelity of the nuclear fragmentation models used. The validation and improvement of these models for SEE rate prediction applications is an ongoing area of research [1,8]. Further information on the implications of nuclear reactions on hardness assurance can be found in [1,6,9].

CHAPTER VI

CONCLUSIONS

Direct charge collection measurements from test structures overlaid with various BEOL materials prove that the presence of high-Z materials (e.g., tungsten) leads to extreme charge collection events through nuclear reactions. For the devices and radiation environments studied, the data show that tungsten nearest the sensitive volume leads to the most extreme charge collection events; however, this finding may not be universally applicable. (E.g., it is conceivable that tungsten further from the sensitive volume could contribute the most to charge collection, if its position caused enough secondary particles to reach their Bragg peaks in the sensitive volume.)

For a fixed incident particle LET, increasing the energy beyond a certain point causes a decrease in nuclear reaction-induced charge collection. This suggests that a worst-case energy exists for SEE susceptibility, which depends on the technology, device layout, critical charge, and the incident ions' fixed LET value. A Monte Carlo simulation approach to determine the worst-case energy has been applied to example bulk-Si and SOI technologies. Nuclear fragmentation simulations suggest that the decrease in charge collection beyond the worst-case energy occurs because the secondary particles produced from very high energy nuclear reactions tend to have lower mass and higher energy than those produced by lower-energy reactions, and are therefore less ionizing.

APPENDIX

DISCRIMINATOR BOARD DESIGN

The Mesytec MPRS-16 preamplifier/shaping amplifier provides a TRIGGER output signal that is typically used to trigger the multichannel analyzer. However, it can be seen in Figure 25 that the TRIGGER is implemented in hardware by summing the signals from the various channels, in groups of four. The sum of the four channels is then fed into a discriminator, and if the pulse exceeds the discriminator limit then TRIGGER is asserted. This implementation assumes that the signals on the separate channels were caused by the same radiation event and are coincident in time. The MPRS-16 is built this way because it is typically used by nuclear physicists to perform PHA on various detectors that are affected by a single radiation event (e.g., detecting each of the secondary particles from a single nuclear spallation reaction in a gold foil). In this situation, it makes sense to discriminate the sum of multiple signals, because the sum of those signals describes the charge deposited by the same radiation event.

In this work, the MPRS-16 is used to perform PHA on 16 detectors in order to increase the observability of nuclear reactions, and the pulses from these separate detectors are not coincident in time because they are caused by separate radiation events. Therefore, it would be inappropriate to perform discrimination on the sum of these signals. The MPRS-16's TRIGGER signal could not be used because it was observed that noise on four channels summed together to exceed the MPRS-16's discriminator setting, so that TRIGGER was frequently asserted when it should not have been.

In order to perform discrimination on each of the 16 channels individually it was necessary to design and build a custom PCB. A simplified diagram of the custom discriminator board is given in Figure 26.

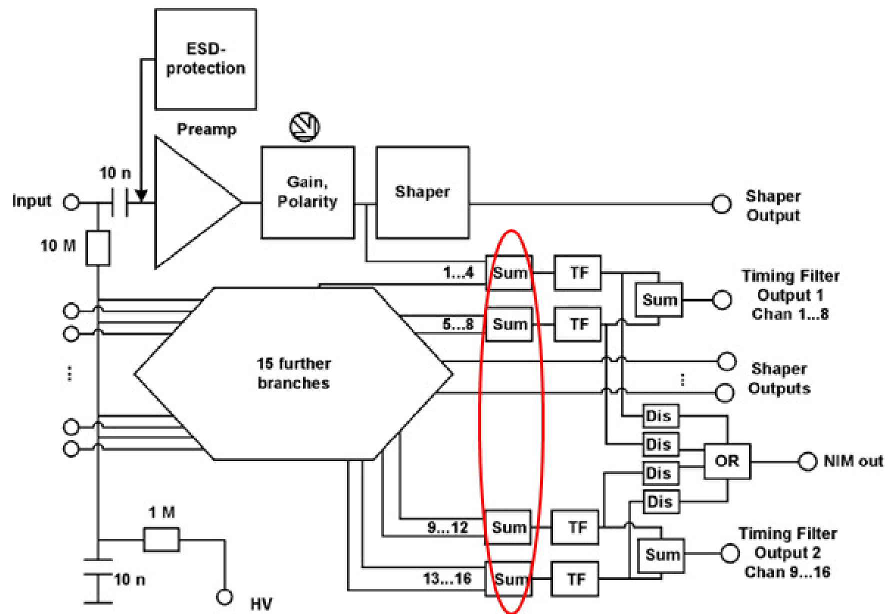

Figure 25: Block diagram of the Mesytec MPRS-16 preamplifier/shaping amplifier. The TRIGGER output (labeled NIM out) cannot be used for this application, because it is produced by summing the signals from the various channels.

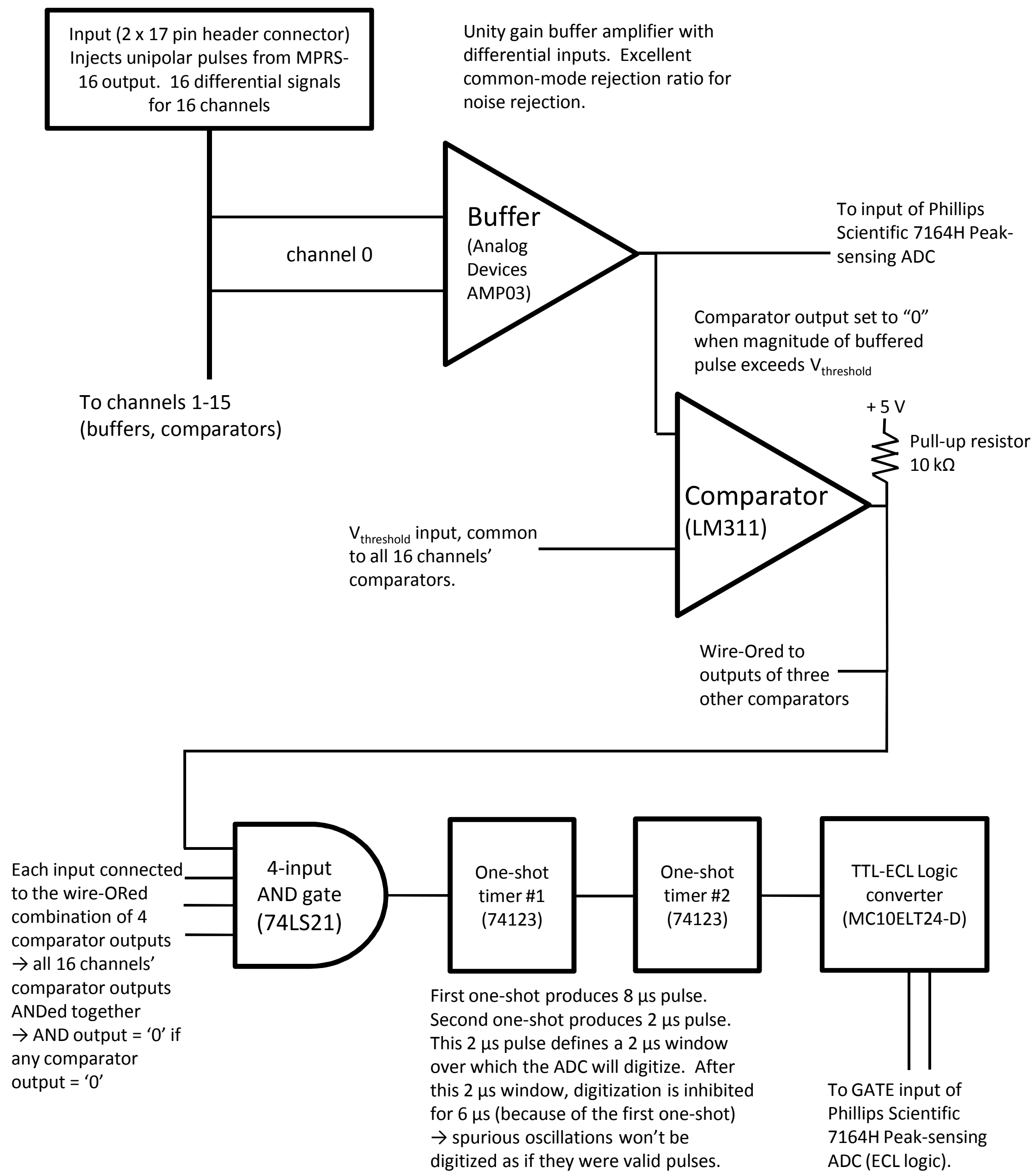

Figure 26: Simplified diagram of the discriminator board with embedded explanations. This circuit produces a trigger signal that tells the ADC to digitize when the magnitude of a pulse on any of the 16 channels exceeds $V_{threshold}$.

REFERENCES

[1] R. A. Reed, R. A. Weller, M. H. Mendenhall, J. -M. Lauenstein, K. M. Warren, J. A. Pellish, R. D. Schrimpf, B. D. Sierawski, L. W. Massengill, P. E. Dodd, M. R. Shaneyfelt, J. A. Felix, J. R. Schwank, N. F. Haddad, R. K. Lawrence, J. H. Bowman, and R. Conde, "Impact of Ion Energy and Species on Single Event Effects Analysis," *IEEE Trans. Nucl. Sci.,* vol. 54, no. 6, pp. 2312 – 2321, Dec. 2007.

[2] C. L. Howe, R. A. Weller, R. A. Reed, M. H. Mendenhall, R. D. Schrimpf, K. M. Warren, D. R. Ball, L. W. Massengill, K. A. LaBel, J. W. Howard, Jr., and N. F. Haddad, "Role of heavy-ion nuclear reactions in determining on-orbit single event error rates," *IEEE Trans. Nucl. Sci.* vol. 52, no. 6, pp. 2182 – 2188, Dec. 2005.

[3] K. M. Warren, R. A. Weller, M. H. Mendenhall, R. A. Reed, D. R. Ball, C. L. Howe, B. D. Olson, M. L. Alles, L. W. Massengill, R. D. Schrimpf, N. F. Haddad, S. E. Doyle, D. McMorrow, J. S. Melinger, and W. T. Lotshaw, "The contribution of nuclear reactions to heavy ion single event upset cross-section measurements in a high-density SEU hardened SRAM," *IEEE Trans. Nucl. Sci.*, vol. 52, no. 6, pp. 2125–2131, Dec. 2005.

[4] J. R. Schwank, M. R. Shaneyfelt, J. Baggio, P. E. Dodd, J. A. Felix, V. Ferlet-Cavrois, P. Paillet, D. Lambert, F. W. Sexton, G. L. Hash, and E. W. Blackmore, "Effects of particle energy on proton-induced single event latchup," *IEEE Trans. Nucl. Sci.*, vol. 52, no. 6, pp. 2622 2629, Dec. 2005.

[5] A. S. Kobayashi, D. R. Ball, K.M. Warren, R. A. Reed, N. Haddad, M. H. Mendenhall, R. D. Schrimpf, and R. A. Weller, "The Effect of Metallization Layers on Single Event Susceptibility," *IEEE Trans. Nucl. Sci.,* vol. 52, no. 6, pp. 2189-2193, Dec. 2005.

[6] P. E. Dodd, J. R. Schwank, M. R. Shaneyfelt, J. A. Felix, P. Paillet, V. Ferlet-Cavrois, J. Baggio, R. A. Reed, K. M. Warren, R. A. Weller, R. D. Schrimpf, G. L. Hash, S. M. Dalton, K. Hirose, H. Saito, "Impact of Heavy Ion Energy and Nuclear Interactions on Single-Event Upset and Latchup in Integrated Circuits," *IEEE Trans. Nuc. Sci.*, vol. 54, no. 6, pp. 2303 - 2311 , Dec. 2007.

[7] G. F. Knoll, *Radiation Detection and Measurement*, 3rd ed. New Jersey: John Wiley & Sons, Inc., 2000, pp. 626-655.

[8] M. A. Clemens, N. A. Dodds, R. A. Weller, M. H. Mendenhall, R. A. Reed, R. D. Schrimpf, T. Koi, D. H. Wright, and M. Asai, "The Effects of Nuclear Fragmentation Models on Single Event Effect Prediction," *IEEE Trans. Nucl. Sci.*, submitted for publication in Dec. 2009 issue.

[9] R. A. Reed, R. A. Weller, R. D. Schrimpf, M. H. Mendenhall, K. M. Warren, and L. W. Massengill, "Implications of Nuclear Reactions for Single Event Effects Test Methods and Analysis," *IEEE Trans. Nucl. Sci.*, vol. 53, no. 6, pp. 3356-3362, Dec. 2006.

[10] W. Shockley, "Problems related to p-n junctions in silicon," *Solid State Electron,* vol. 2, pp. 35-67, 1961.

[11] V. Ferlet-Cavrois, P. Paillet, J. Schwank, G. Vizkelethy, M. Shaneyfelt, J. Baggio, A. Torres, and O. Flament, "Charge collection by capacitive influence through isolation oxides," *IEEE Trans. Nucl. Sci.*, vol. 50, no. 6, pp. 2208-2218, Dec. 2003

[12] J. R. Schwank, V. Ferlet-Cavrois, P. E. Dodd, M. R. Shaneyfelt, G. Vizkelethy, P. Paillet, and O. Flament, "Analysis of heavy-ion induced charge collection mechanisms in SOI circuits," *Solid-State Electronics*, vol. 48, pp. 1027-1044, Jun. 2004

[13] "Python Laboratory Operations Toolkit," SourceForge.net, 2009 [Online]. Available: http://sourceforge.net/projects/pythonlabtools/

[14] "Passage of particles through matter," Particle Data Group, 2005 [Online]. Available: http://pdg.lbl.gov/2005/reviews/passagerpp.pdf

[15] J. F. Ziegler, J. P. Biersack, and U. Littmark*, The Stopping and Range of Ions in Solids*. New York: Pergammon, 1985, vol. 1.

[16] J. H. Adams Jr., R. Silberberg, and C. H. Tsao, "Cosmic Ray Effects on Microelectronics," *IEEE Trans. Nucl. Sci.*, vol. ns-29, no. 1, pp. 169-172, Feb. 1982.

[17] R. A. Reed, J. Kinnison, J. C. Pickel, S. Buchner, P. W. Marshall, S. Kniffin, and K. A. LaBel, "Single-Event Effects Ground Testing and On-Orbit Rate Prediction Methods: The Past, Present, and Future," *IEEE Trans. Nucl. Sci.,* vol. 50, no. 3, pp. 622-634, Jun. 2003.